Pergamon

Pyritization processes and greigite formation in the advancing sulfidization front in the Upper Pleistocene sediments of the Black Sea

Lev N. Neretin,[1,*] Michael E. Böttcher,[1] Bo B. Jørgensen,[1] Igor I. Volkov,[2] Holger Lüschen,[3] and Katharina Hilgenfeldt[4]

[1]Max Planck Institute for Marine Microbiology, Celsiusstrasse 1, D-28359, Bremen, Germany
[2]P. P. Shirshov Institute of Oceanology of Russian Academy of Sciences, Nakhimovskiy prosp., 36, 117851 Moscow, Russia
[3]Institute of Chemistry and Biology of the Marine Environment (ICBM), University of Oldenburg, P.O. Box 2503, D-26111 Oldenburg, Germany
[4]Fachbereich Geowissenschaften, Universität Bremen, Postfach 330 440, 28334 Bremen, Germany

Abstract—Pyritization in late Pleistocene sediments of the Black Sea is driven by sulfide formed during anaerobic methane oxidation. A sulfidization front is formed by the opposing gradients of sulfide and dissolved iron. The sulfidization processes are controlled by the diffusion flux of sulfide from above and by the solid reactive iron content. Two processes of diffusion-limited pyrite formation were identified. The first process includes pyrite precipitation with the accumulation of iron sulfide precursors with the average chemical composition of FeS_n (n = 1.10–1.29), including greigite. Elemental sulfur and polysulfides, formed from H_2S by a reductive dissolution of Fe(III)-containing minerals, serve as intermediates to convert iron sulfides into pyrite. In the second process, a "direct" pyrite precipitation occurs through prolonged exposure of iron-containing minerals to dissolved sulfide. Methane-driven sulfate reduction at depth causes a progressive formation of pyrite with a $\delta^{34}S$ of up to +15.0‰. The S-isotopic composition of FeS_2 evolves due to contributions of different sulfur pools formed at different times. Steady-state model calculations for the advancement of the sulfidization front showed that the process started at the Pleistocene/Holocene transition between 6360 and 11 600 yr BP. Our study highlights the importance of anaerobic methane oxidation in generating and maintaining S-enriched layers in marine sediments and has paleoenvironmental implications. *Copyright © 2004 Elsevier Ltd*

1. INTRODUCTION

The Black Sea changed from freshwater to brackish conditions in association with the Pleistocene/Holocene transition (e.g., Jones and Gagnon, 1994). This transition was accompanied by a change from a low to a high sulfate environment. An organic carbon-rich sapropel deposited above organic carbon-poor limnic clay sediment. Earlier studies suggested that the diffusion of sulfide formed in situ during sulfate reduction in the sapropel caused a progressive sulfidization of the underlying freshwater sediments with high pore water and solid phase iron contents (Volkov, 1964; Berner, 1974). Consequently, iron sulfide-rich layers were formed in the upper limnic sediment, occurring as black layers of 20 to 150 cm thickness. These layers, discovered in the 1950s, are rich in amorphous iron sulfide (FeS_{am}). The FeS_{am}-rich layer (or "hydrotroilite layer" in the earlier Russian literature) is present as a single layer at the periphery of the basin and splits into several layers in the central part of the basin (Strakhov, 1963).

Iron sulfides are operationally defined as acid-volatile sulfides (AVS) that dissolve during hot 6 N HCl treatment and include amorphous FeS (FeS_{am}), mackinawite (tetragonal FeS) and greigite (Fe_3S_4) (Chanton and Martens, 1985; Morse and Cornwell, 1987). AVS enrichments at depth in marine sediments under anoxic conditions were reported for the Arabian Sea (Volkov et al., 1981) and for sediments of Saguenay Fjord

sediments (Gagnon et al., 1995), and were presumably formed from hydrogen sulfide produced by bacterial sulfate reduction. A postsedimentation migration of hydrogen sulfide, as has been demonstrated for limnic clays of the Black Sea, has also been described as the main mechanism of sulfidization of Ancylus clays in the Baltic Sea (Boesen and Postma, 1988; Böttcher and Lepland, 2000), sediments of the Kau Bay in Indonesia (Middelburg, 1991), hemipelagic sediments underlying sapropels in the eastern Mediterranean (Passier et al., 1996, 1999), deep sediments of the Amazon Fan (Kasten et al., 1998), and, more recently, of late Pleistocene sediments of the Cariaco Basin, Venezuela (Lyons et al., 2003).

AVS can be formed during reductive dissolution of iron hydroxides (Pyzik and Sommer, 1981; Afonso and Stumm, 1992; Rickard, 1995) or by reaction of ferric iron in clay minerals (Rozenson and Heller-Kallai, 1976) during reduction with sulfide. Elemental sulfur, polysulfides and thiosulfate have been observed to be intermediate products in these reactions (Pyzik and Sommer, 1981; Peiffer et al., 1992).

Pyrite is the most stable iron-sulfide mineral in marine sediments. The importance of an iron monosulfide precursor to pyrite formation has been recognized for many years (Berner, 1970; Jørgensen, 1977; Volkov, 1984; Boesen and Postma, 1988; Canfield et al., 1992; Wilkin and Barnes, 1996; Lyons, 1997; Hurtgen et al., 1999; Benning et al., 2000). Studies in the laboratory (Berner, 1970; Rickard, 1975; Luther, 1991; Schoonen and Barnes, 1991a,b; Kozerenko et al., 1995; Wilkin and Barnes, 1996; Benning et al., 2000) and in the field (Volkov, 1984; Middelburg, 1991; Gagnon et al., 1995; Lyons, 1997)
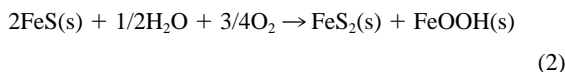
* Author to whom correspondence should be addressed (lneretin@mpi-bremen.de).

have shown that an oxidant is necessary to produce pyrite from an iron monosulfide precursor. Several mechanisms of pyrite formation at low temperatures were proposed:

A. "Polysulfide pathway" (e.g., Luther, 1991; Rickard, 1975)

$$FeS(s) + S^0(s) \rightarrow FeS_2(s)$$

$$FeS(s) + S_n^{2-} \rightarrow FeS_2(s) + S_{n-1}^{2-} \qquad (1)$$
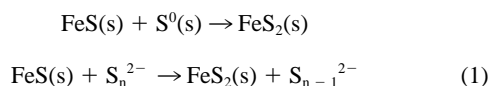
B. "Ferrous iron loss pathway" (Wilkin and Barnes, 1996)

$$2FeS(s) + 1/2H_2O + 3/4O_2 \rightarrow FeS_2(s) + FeOOH(s)$$
$$(2)$$

C. "H₂S pathway" (Drobner et al., 1990; Rickard, 1997; Rickard and Luther, 1997)

$$[FeS](aq) + H_2S \rightarrow FeS_2(s) + H_2 \qquad (3)$$

The role of reduced sulfur intermediates in pyrite formation from FeS in marine sediments is well known (Eqns. 1 and 2) (Volkov, 1964; Berner, 1970; Sweeney and Kaplan, 1973; Rickard, 1975; Luther, 1991; Schoonen and Barnes, 1991a,b; Wilkin and Barnes, 1996). In most of these studies, elemental sulfur (or polysulfides) has been suggested to be the most probable candidate. In natural environments, the persistence of iron monosulfide is controlled by a complex interplay of different factors, including sedimentation rate, existence of the intermediate sulfur species, or presence of H₂S in the pore water. Hurtgen et al. (1999) argued that under conditions promoting the spatial separation of FeS and sulfur intermediates, a direct transformation of FeS to FeS₂, "H₂S pathway" (Eqn. 3), may occur.

The oxidation of FeS(s) to pyrite involves a dissolved phase [FeS](aq) (Rickard and Luther, 1997). However, under certain conditions, the FeS is converted to greigite and not to pyrite. The oxidation of FeS to Fe₃S₄ is most probably a solid-state reaction (Postfai et al., 1998).

In contrast to "normal" marine sediments deposited under oxic conditions, where pyrite forms exclusively within the sediment, in euxinic environments like the Black Sea pyritization can also proceed in the water column (syngenetic pyrite) and at or below the sediment-water interface (diagenetic pyrite). Syngenetic pyrite has been suggested to be the main component of the pyrite pool in the uppermost Holocene laminated sediments (Unit I) in the central Black Sea (e.g., Calvert et al., 1996; Canfield et al., 1996; Lyons, 1997; Wilkin et al., 1997). However, there is also strong evidence for a significant contribution of a diagenetic component (Volkov, 1984; Neretin et al., 2001) in nonturbiditic sediments of the central basin.

In earlier studies of iron-sulfur diagenesis in sediments deposited during the late Pleistocene–early Holocene (e.g., Vinogradov et al., 1962; Volkov, 1964; 1984; Berner, 1974; Calvert et al., 1996; Wilkin and Arthur, 2001), high resolution data for iron and for both solid and pore water sulfur species together with their isotope signatures were not concurrently obtained. The data could therefore not support mass balance calculations for iron and sulfur species during non–steady-state diagenesis at the Pleistocene/Holocene transition and did not clearly delineate the sulfur source for pyritization of the limnic sediments.

Jørgensen et al. (2004) demonstrated that methane-driven sulfate reduction at depth in the Black Sea sediments causes the formation of H₂S and subsequent downward advancement of a sulfidization front in the upper limnic sediments with accompanying sulfur immobilization. In the present paper, we elaborate the suggested model with the aim to explain the origin and chemistry of iron-sulfide–rich layers and the process of pyritization. Furthermore, we reconstruct the evolution of the sulfidization front under steady-state model assumptions.

2. MATERIALS AND METHODS

2.1. Sampling

Samples were collected at Station 7 (43°31.′32N, 30°13.′84E) in the middle part of the continental slope at a water depth of 1176 m during a cruise of R/V *Petr Kotzov* in 1997. At the station, several 10 cm (I.D.) multicores and two 12 cm (I.D.) gravity cores were collected. Cores obtained with the multicorer were sectioned onboard the ship immediately after recovery, preserved as described for the gravity core, and analyzed within several hours onboard the ship for AVS, TRS (TRS = Σ(AVS + S⁰ + FeS₂), and reactive iron. One gravity core was sealed with caps and tape and then transported to Bremen, where it was kept at 4°C for a couple of months. It was then split, and samples were taken from the inner part of the core at depth intervals of 2–10 cm using syringes with luer end removed. For the analyses of reduced sulfur species, the samples were placed in 50 mL centrifuge tubes filled with 10 mL of 20% (w/v) Zn acetate solution to prevent oxidation of dissolved sulfide and inhibit bacterial activity during storage. For the determinations of water content, solid phase reactive iron, total and inorganic carbon, and total S, Fe, and Al, samples were preserved at −20°C without addition of Zn acetate. Visual observation did not indicate oxidation of sulfur species during storage and sampling (no indication for the presence of iron oxides in AVS-rich layers). This was further confirmed by independent measurements of samples preserved onboard from a core recovered at the same site and analyzed in the Laboratory of Geochemistry of the Shirshov Institute of Oceanology RAS (Moscow, Russia) (I. Volkov, unpublished data). Depths in the two cores were correlated using stratigraphical descriptions, pore water analysis, and by comparing the δ³⁴S values of Cr(II) reducible sulfur.

2.2. Pore-Water Analyses

Sediment pore water sampling and analyses were done as described by Jørgensen et al. (2001). Briefly, after sampling with syringes with the ends removed, pore water was extracted within 30 min by sediment squeezing through 0.45 μm membrane filters under 3–5 bar N₂ pressure. H₂S was fixed in 2% (w/v) ZnCl₂ and analyzed by the methylene blue assay (Cline, 1969). Sulfate concentrations were determined by nonsuppressed anion exchange chromatography (Waters 510 HPLC Pump, Waters IC-Pak column, Waters 430 conductivity detector) using 1 mM isophthalic acid with 10% (v/v) methanol as the eluent. Samples for methane analyses were preserved in 0.1% (w/v) NaOH-containing serum vials and analyzed onboard the ship by gas chromatography (Beckmann 5890 with FID).

Sulfate and sulfide concentrations in pore water are reported as molarity. Methane concentrations were recalculated to μmol per liter of pore water based on sediment porosity (Jørgensen et al., 2001).

2.3. Solid Phase Analyses

Water content was determined gravimetrically upon freeze-drying. Total carbon (TC) and total sulfur (TS) were measured in freeze-dried samples using a LECO analyzer. Total inorganic carbon (TIC) was analyzed on a CM 5012 CO₂ coulometer with a CM 5130 acidification module. The TIC was recalculated to the equivalent amount of CaCO₃. Total organic carbon (TOC) was calculated as the difference between TC and TIC. Total Fe and Al were measured by XRF spectroscopy (SD < 1%) on fused borate glass beads using a Philips PW 2400 XRF spectrometer at the Institute of Chemistry and Biology of the Marine Environment, University of Oldenburg. Solid phase compositions are given in % dw (% dry weight) without correction for the salt content.

Magnetic sulfide micronodules were recovered at depths of 324–329 and 343 cmbsf. The mineralogy of the nodule from 343 cmbsf depth was analyzed using powder X-Ray Diffraction (XRD) between 2° and 80° 2θ at a speed of 0.02° 2θ s^{-1}.

Reactive iron (Fe$_{react}$) was extracted using 50 mL Na dithionite with a NaAc buffer and 0.1 g of dry sediment (Canfield, 1989). This iron fraction represents the sum of iron derived from iron carbonates, acid volatile sulfides, and amorphous oxyhydroxides (Canfield, 1989; Raiswell et al., 1994). By definition this is an iron pool available for relatively fast diagenetic transformations in sediments and particularly for reactions with H$_2$S. The Na dithionite-Na acetate extraction was prepared from 2 g of Na dithionite/50 mL of acetate buffer (pH = 4.8) made from 0.35 M acetic acid and 0.2 M Na acetate. The extraction was performed for 4 h with gentle shaking. The supernatant was filtered through a 0.45 μm membrane filter, fivefold diluted with dH$_2$O, and the Fe content was analyzed by Atomic Absorption Spectrometry (SD between parallel samples <5%) (Perkin Elmer 3110).

Reduced sulfur species were extracted following the scheme developed by Zhabina and Volkov (1978) with some modifications. Replicate analyses of marine samples using this method generally yield a reproducibility of ±2% or better (Lyons et al., 2003). Between 0.5 and 2 g wet sediment were used for the analysis. Extraction of AVS was performed under N$_2$ with hot 6 N HCl for 30 min. Elemental sulfur, S^0, was extracted after the AVS extraction and subsequently pyrite, FeS$_2$, was extracted in a boiling 1 M CrCl$_2$ acidic (3 N HCl) solution for 1 h.

Two acetone extractions of elemental sulfur, before and after the HCl treatment, were only performed in the upper limnic sediment (the upper part of Unit III), rich in AVS. These sulfur pools were defined operationally as elemental sulfur, S^0, (see above) and elemental sulfur formed from acid volatile sulfides (AVS), S$^0_{AVS}$. In both cases, elemental sulfur was extracted by acetone in a Soxhlet apparatus for 8 h. After extraction, the S^0 was reduced by 1 M CrCl$_2$ in 3 N HCl (Zhabina and Volkov, 1978) under a continuous flow of N$_2$ for 30 min at room temperature, and the evolved H$_2$S was trapped in 20% (w/v) Zn acetate.

For quantification of AVS and pyrite sulfur, liberated H$_2$S was also trapped in 20% Zn acetate. After extractions, a ZnS aliquot was subsampled for H$_2$S determination by the methylene blue assay (Cline, 1969), and the remainder was acidified with 6 N HCl under N$_2$ at room temperature. The evolved H$_2$S was trapped in 6% (w/v) AgNO$_3$. After filtration through a 0.45 μm membrane filter, Ag$_2$S samples were air dried at 60°C for several hours and used for sulfur isotope measurements.

2.4. Sulfur Isotopic Measurements

The isotopic composition of sulfur species was determined by combustion isotope-ratio monitoring mass-spectrometry as described by Böttcher et al. (1998b). Sulfide and sulfate samples were combusted in a Carlo Erba Elemental Analyzer (EA 1108) connected to EA via a Finnigan MAT ConFlo II interface to a Finnigan MAT 252 triple collector mass-spectrometer. The isotope ratios are expressed in the usual δ-notation as permil (‰) relative to the SO$_2$-based Vienna Canyon Diablo Troilite (V-CDT) standard:

$$\delta^{34}S = (R_{sample}/R_{VCDT} - 1) \times 1000, \quad (4)$$

where R = ^{34}S/^{32}S. Reproducibility of all measurements was better than ±0.2‰. IAEA silver sulfide and barium sulfate standards were used to calibrate the mass spectrometer.

2.5. Magnetic Susceptibility Measurements

Magnetic susceptibility (χ) is one of the most commonly used mineral magnetic parameters, which is the ratio of induced magnetization acquired by the sample in the presence of a weak magnetic field, to the applied field itself (Verosub and Roberts, 1995). The magnetic susceptibility is directly proportional to the quantity and grain size of ferro- or ferrimagnetic minerals. Natural remanent magnetization (NRM) in marine sulfide-bearing sediments is mostly due to the presence of greigite and pyrrhotite (Fe$_7$S$_8$). Magnetic susceptibility data were acquired on a half split core at 1 cm intervals using a Bartington MS2 susceptibility system equipped with a MS2E1 surface scanning spot sensor.
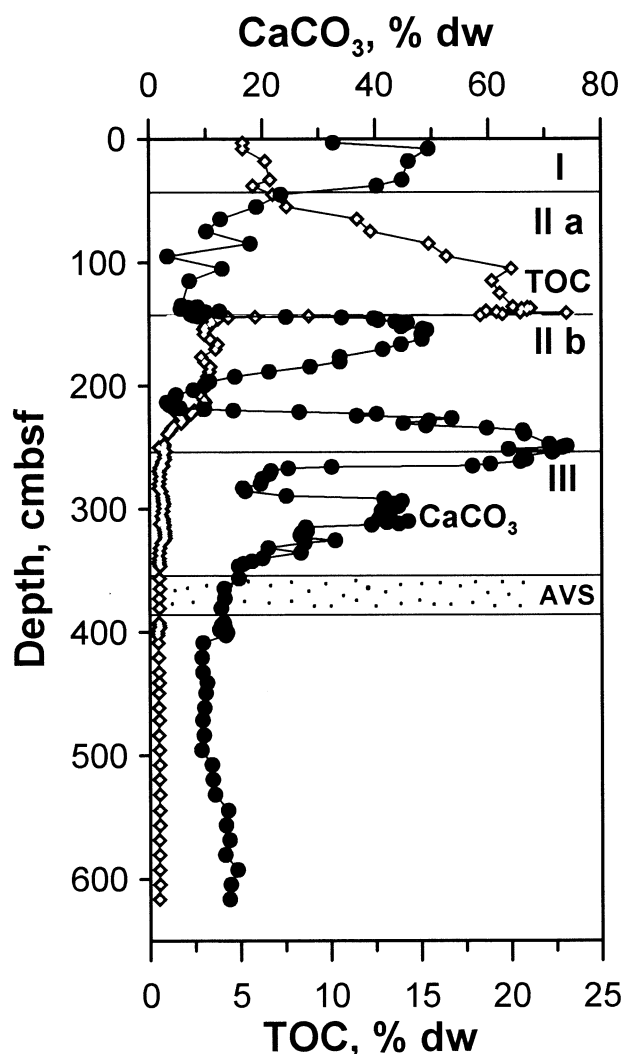

Fig. 1. Depth distributions of TOC (diamonds) and CaCO$_3$ (circles). The AVS-rich layer in this and other figures is shown by a dotted area.

3. RESULTS

3.1. Lithology, TOC, and CaCO$_3$

Detailed sediment stratigraphy for the station is presented in a companion paper by Jørgensen et al. (in press). Briefly, the stratigraphy of the gravity core comprises four units (Fig. 1 as defined by Hay et al., 1991). The upper Unit I represents laminated, coccolith-bearing marls. Unit I (43 cmbsf) had a TOC content of 3.7–4.8% and 32.6–50.3% CaCO$_3$. This layer was recovered by a multicorer. Unit II sediments are divided into two parts: Unit IIa and Unit IIb. Unit IIa (43–143 cmbsf) is a well-defined laminated sapropel with an organic carbon content of up to 21.1% (mean 18.7%) and a CaCO$_3$ content of 3.2–23.3%. Unit IIb (143–254 cmbsf) is a sapropelic layer with a TOC content of 0.81–3.70% and CaCO$_3$ concentrations varying between ca. 3.1 and 73.9%. The depth interval of 250–319 cmbsf probably contained turbidite sequences based on Zr/Al and Ti/Al ratios measured by X-Ray Fluorescence (XRF) (Lüschen, 1998). Freshwater muds, from 254 cmbsf to the base of
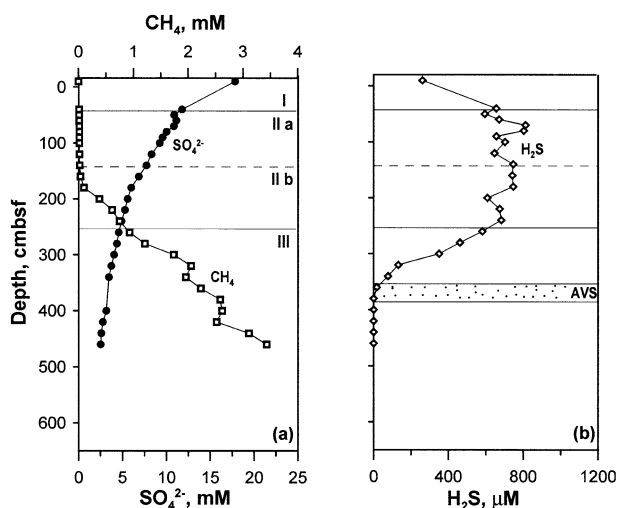
Fig. 2. Depth distributions of pore water constituents: sulfate and methane (a) and sulfide (b). The uppermost values are measurements from water above the sediment. Data are from Jørgensen et al. (2001) and Jørgensen et al. (in press).
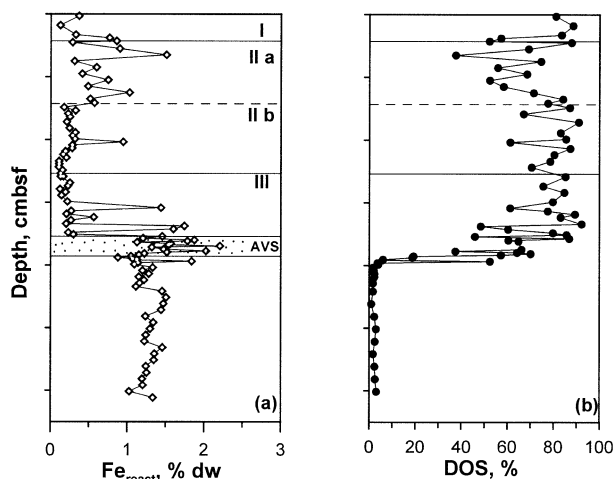

Fig. 3. Depth distributions of reactive iron Fe_{react} (a) and DOS (b).

3.3. Reactive Iron Content and DOS

The extent of sulfidization of available iron may be expressed as the degree of sulfidization (DOS), defined as DOS = $[(Fe\text{-}FeS_2 + Fe\text{-}FeS)/(Fe\text{-}FeS_2 + Fe_{react})] \times 100\%$ (Boesen and Postma, 1988).

The vertical distributions of reactive iron and DOS are inverse (Fig. 3). Typical limnic clays below the FeS_{am}-rich layer had the lowest DOS values of 0.9 to 3.9% and, accordingly, the highest average Fe_{react} content of $1.07 \pm 0.55(1\sigma)$ %. Reactive iron was still present at ca. 2% in the FeS_{am}-rich layer. Pyrite sulfur was the dominant form of total reduced sulfur above the AVS-rich layer and the Fe_{react} content was 0.3–0.5%. The DOS in these upper layers, including the modern marine sediments, varied between 38 and 92% with an average of $72 \pm 15(\sigma)$ %. The vertical distribution of reactive iron essentially followed the vertical distribution of total iron.

3.4. Reduced Inorganic Sulfur Species

Depth distributions of acid volatile sulfide (S_{AVS}), pyrite sulfur (S_{FeS2}), elemental sulfur (S^0) and elemental sulfur formed during AVS extraction (S^0_{AVS}) are shown in Figures 4 and 5a. The AVS concentrations had two pronounced maxima: one in the lower part of Unit IIa, with an AVS content of 0.22%, and a second maximum of 0.66% in Unit III. The second maximum defines the FeS_{am}-rich layer. Both maxima were accompanied by increased S^0 concentrations.

For most of the core above the FeS_{am}-rich layer, pyrite sulfur comprised more than 80% of the total reduced sulfur (TRS) (data not shown) with concentrations in the range of 0.5–2%. The TRS concentration decreased abruptly from 0.41% at the top of the FeS_{am}-rich layer to 0.02% at the base of the layer. Most of the reduced sulfur in the black band (~80%) was AVS sulfur. The total FeS_2 and AVS contents were below 0.1% in the limnic clays below the FeS_{am}-rich layer, indicate a sulfate-limited environment during late Pleistocene.
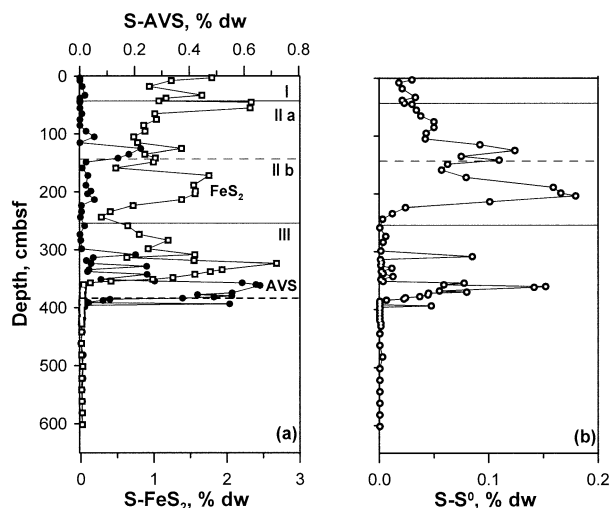
the core at 619 cmbsf, correspond to Unit III and had TOC and $CaCO_3$ contents of 0.4 to 0.9% and 8.7 to 26.3%, respectively. In the upper part of Unit III, sediments were slightly laminated, clay-rich muds with black bands of mm thickness. A well-defined FeS_{am}-rich layer occurred in the depth range from 354 to 386 cmbsf. The lower part of Unit III, below 386 cmbsf, represented the limnic sediment unchanged by secondary sulfidization.

3.2. Sulfate, Methane, and Hydrogen Sulfide in Sediment Pore Waters

The sulfate profile had a concave-down shape, and the sulfate concentration in the lower part of the core was ~2.5 mM relative to 17.8 mM in the bottom water (Fig. 2a). There was a subtle change in the sulfate gradient at the depth of methane onset. From 164 cmbsf downwards, the methane concentration increased steeply with depth to more than 3.4 mM at 460 cmbsf, thus showing a broad overlap between sulfate and methane. The upper boundary of the sulfate/methane interface may be assigned to the depth of 160–180 cmbsf; the lower boundary is undefined due to the incomplete sulfate consumption. Although, sulfate and methane overlap broadly at Station 7, modeling of the sulfate and methane profiles showed an increased rate of sulfate reduction (deep sulfide production) in the zone of anaerobic methane oxidation (AMO) (Jørgensen et al., 2001).

The H_2S concentration in the bottom water was 295 μM. The uppermost sediment recovered by the gravity core (40 cmbsf) had an H_2S content of 655 μM. Sulfide concentrations did not change significantly over the depth range between 40 cmbsf and 240 cmbsf, where the average concentration was $695 \pm 66(1\sigma)$ μM (Fig. 2b). Below 240 cm H_2S decreased to less than 1 μM at the base of the FeS_{am}-rich layer through reaction with Fe.

Fig. 4. Depth distributions of AVS, FeS_2 (a) and S^0 (b). The location of the present sulfidization front is shown by a dotted line on panel (a).

3.5. Susceptibility

The susceptibility profile is presented in Figure 5b for the depth interval of 250–450 cmbsf. Below ca. 350 cmbsf, the average susceptibility in the limnic sediment not modified by the secondary diagenetic overprint was $(124 \pm 23)\ 10^{-6}$ SI. Susceptibility maxima of 10–100 times above background values were recorded at depths of 325, 334, 341 and 345 cmbsf. At these depths we found magnetic micronodules of <2 mm diameter (Fig. 5b) and peaks of S^0_{AVS} were observed (Fig. 5a). The XRD spectrum of a nodule recovered at 343 cmbsf indicated the presence of greigite and pyrite (Fig. 6). Therefore, peaks in the natural remanent magnetization spectrum of sediments overlying the FeS_{am}-rich layer are explained by the presence of greigite.
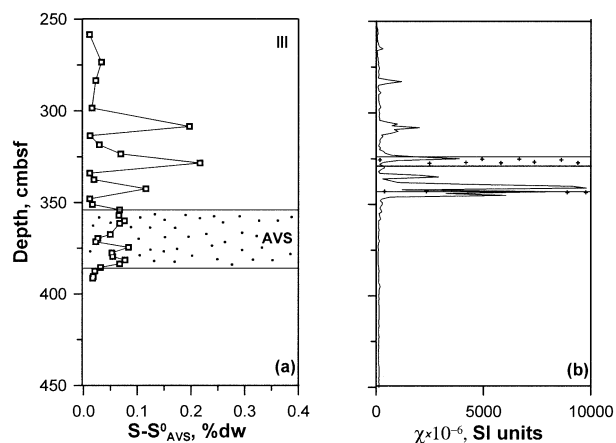

Fig. 6. XRD spectrum of a nodule from 343 cmbsf documenting the presence of both greigite and pyrite.

3.6. Sulfur Isotope Composition of Reduced Sulfur Species

Our data for $\delta^{34}S$-FeS_2 showed that the sulfur was relatively depleted in ^{34}S from the sediment surface to the base of Unit IIa, with values increasing from −37.4‰ to −22.7‰ (Fig. 7a). The isotope values in the upper part of Unit IIa were close to $\delta^{34}S$-FeS_2 values previously recorded in Unit I (e.g., Lyons, 1997; Neretin et al., 2001). Unit IIb sediments are characterized by a significant scatter in $\delta^{34}S$-FeS_2 values, which ranged between −31.2‰ and −11.0‰. At the brackish/freshwater interface (Unit IIb/Unit III boundary), $\delta^{34}S$-FeS_2 increased abruptly from −18.9‰ to +15.0‰ within several centimeters. Pyrite sulfur was then again progressively enriched in the lighter isotope with depth from +15.0‰ to −9.0‰ in the limnic sediment.

The general trend of the $\delta^{34}S$-AVS depth distribution was similar to that of pyrite sulfur (Fig. 7a). The AVS isotope composition was in most cases heavier than that of FeS_2, by up to 20‰ at some depths. The elemental sulfur (S^0) isotope composition changed from −19.0‰ in the sapropel to a maximum of +16.2‰ in the upper freshwater sediments above the

Fig. 5. Depth distributions of S^0_{AVS} (a) and magnetic volume susceptibility χ (b) in the layer 250–450 cmbsf. Nodules with magnetic properties were recovered from the depths 324–329 cmbsf and 343 cmbsf (in (b) shown as crosses).
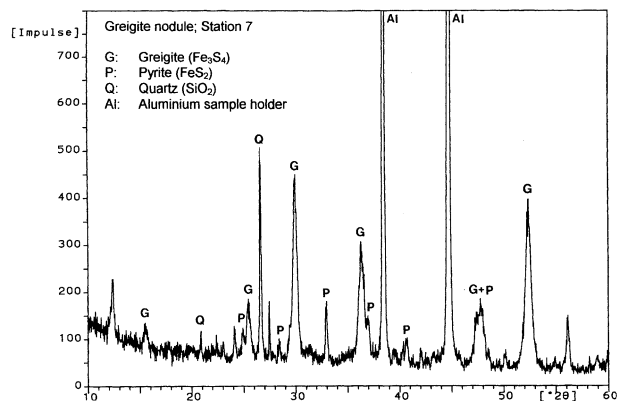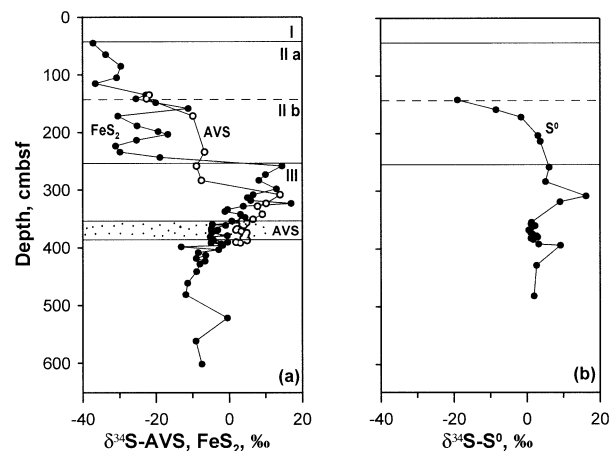

Fig. 7. Depth distributions of $\delta^{34}S$-AVS and $\delta^{34}S$-FeS_2 (a) and $\delta^{34}S$-S^0 (b).
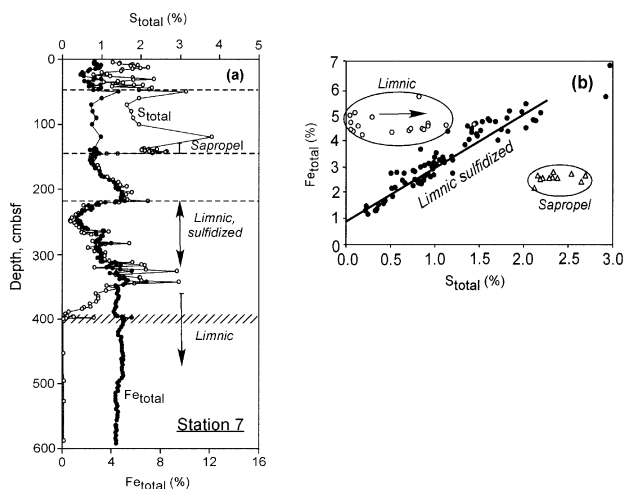
Fig. 8. The vertical distribution of total iron and total sulfur (Fe_{total} only below 135 cmbsf) (a). Fe_{total} versus S_{total} showing the high sulfur content in the sapropel, the positive correlation of iron and sulfur in the sulfidized limnic sediment, and the relatively low content in the limnic part below the sulfidization front (the arrow indicates gradual sulfidization) (b).

FeS_{am}-rich layer (Fig. 7b). The $\delta^{34}S$ of S^0 in the FeS_{am}-rich layer between -2.5 and $+2.5$‰ was similar to the sulfur isotope compositions of AVS and FeS_2.

3.7. Total Iron and Sulfur Speciation

Total sulfur increased with depth below the sediment surface and reached peaks of 3.2% and 3.9% in the upper and lower part of the sapropel, respectively (Fig. 8a). In the sulfidized brackish to limnic Unit IIb–III sediment below 90 cm, S_{total} was around 1%. It dropped in the lower part of the pyritized zone between 340 and 384 cmbsf. Below the FeS_{am}-rich layer, where the H_2S diffusion front had not yet penetrated, the S_{total} content was very low, 0.05–0.1%, a range characteristic of limnic sediments and was consistent with the AVS and pyrite data reported earlier.

The total sulfur content in the sulfidized Upper Pleistocene sediments below the sapropel was governed by the amount of reactive iron available to form pyrite, rather than by the amount of H_2S produced. This is shown by a detailed comparison between the distributions of total sulfur and total iron (Fig. 8a). The sulfidization front has reached ca. 384 cmbsf (Fig. 5a), and between 150 and 350 cmbsf the total sulfur concentration closely followed the variations in total iron (Fig. 8a). Throughout this depth interval the H_2S concentration was high, 200–700 μM (Fig. 2), and thus not limiting for the formation of iron-sulfur minerals. Below the sulfidized zone the limnic sediment had a very constant Fe_{total} concentration of 4–5%.

The close Fe_{total}/S_{total} correlation in the sulfidized limnic sediment is shown in Figure 8b. Given the excess of H_2S, we conclude that the reactivity of iron minerals here govern the degree of sulfidization (Fig. 3). The scatter plot in Figure 8b also shows distinctly the sulfur-rich sapropel, where between 13 and 59% of the total sulfur is organically bound (Jørgensen et al., in press). The plot also illustrates that the limnic sediment is undergoing a progressive sulfidization in the transition zone starting at the lower boundary of free H_2S at ca. 384 cmbsf and going towards ca 350 cmbsf (arrow). The upper limnic sediment above ca. 320 cmbsf is characterized by lower Fe_{total} content and slightly higher Fe_{total}/Al ratio (Table 1) than sediments below due to turbidites influence.

Summarizing, our geochemical data record the sedimentary evolution from lake to sapropel to modern Unit I sediments. The brackish/limnic interface is defined as the boundary between Unit IIb and Unit III. Pyritization processes above this interface are iron-limited as indicated by the high H_2S concentrations, the high DOS and the pyrite contents in the range of 1–2%. The pyrite sulfur comprises more than 80% of the TRS pool. The upper part of Unit III represents diagenetically overprinted limnic clays. These upper limnic sediments are characterized by DOS, TRS and S_{total} values similar to those in the overlying sediments, but the ^{34}S enrichment provides strong evidence for a secondary overprint. The combined H_2S, SO_4^{2-} and CH_4 profiles and the ^{34}S enrichment of solid phase sulfur species suggest that the H_2S source is derived from anaerobic methane oxidation (Jørgensen et al., 2001 Jørgensen et al., in press). Migration of sulfide downward results in significant sulfidization of sulfur-limited clays and the formation of a FeS_{am}-rich layer. Typical limnic clays below this layer have very low TRS and S_{total} contents and very low DOS, high

Table 1. Fe species ratios to total Fe and Al and DOS at Station 7.[a]

Stratigraphy unit (depth interval, cmbsf)	$Fe_{AVS+pyr}/Fe_{total}$ (%) (1)	DOS (%) (2)	Fe_{total}/Al (3)	$Fe_{dith+pyr}/Al$ (4)	$Fe_{dith+pyr}/Fe_{total}$ (5)
Unit IIb (149–249)	16.7–51.6 (10)	61–91 (10)	0.48–0.55 (19)	0.14–0.30 (10)	24.9–56.7 (10)
	30.1 ± 10.2	79 ± 10	0.52 ± 0.01	0.20 ± 0.05	37.7 ± 10.1
Upper Unit III (254–351)	13.3–54.7 (13)	48–92 (13)	0.50–0.83 (17)	0.11–0.41 (13)	17.2–69.5 (13)
	31.3 ± 11.6	77 ± 11	0.58 ± 0.06	0.24 ± 0.10	41.5 ± 16.2
FeS_{am}-rich layer (354–386)	15.9–25.9 (13)	19–87 (13)	0.48–0.53 (11)	0.12–0.26 (13)	27.9–47.5 (13)
	21.1 ± 4.4	57 ± 19	0.51 ± 0.02	0.18 ± 0.04	35.2 ± 6.4
Lower Unit III (388–612)	≪1.0	0.9–3.9 (21)	0.48–0.70 (30)	0.10–0.23 (21)	20.9–32.9 (21)
		2.3 ± 0.6	0.52 ± 0.02	0.14 ± 0.02	26.7 ± 2.1

[a] $\dfrac{\text{interval (number of measurements)}}{\text{average}\pm\text{99\% CI}} \Big\}$.

reactive iron concentrations and relatively high $\delta^{34}S$ values, all of which indicate their deposition under sulfate-limited and iron-rich conditions in the Pleistocene lake.

4. DISCUSSION

4.1. Sulfur Relationships

The depth distributions of solid sulfur species in the upper part of Unit III sediments (Fig. 4) indicate AVS formation and their conversion into pyrite driven by a progressive diffusion of hydrogen sulfide (Fig. 2b). Given that the concentration of reduced sulfur in the initially nonsulfidized limnic clays was negligible (DOS < 1%), and depositional conditions did not change significantly over the late Pleistocene, the original composition of the detrital iron pool can be assumed as constant for all depths of the upper Unit III clays, including the hydrotrolilite layer. Thus, the amount of pyrite formed in the upper part of Unit III by AVS formation linked to H_2S diffusion and by conversion of AVS can be estimated.

The upper 129 cm of the Unit III sediments are sulfidized (pyritized) (Fig. 3b). The upper 100 cm of Unit III (254–354 cmbsf) contain FeS_2 representing more than 90% of TRS (data not shown), and the underlying FeS_{am}-rich layer has a width of 32 cm. The solid sulfide (AVS + FeS_2) inventory, S_{inv}, i.e., total amount of accumulated S summed in a specified sediment thickness (Z0-Z1) below one cm², can be calculated by the following formula (Passier et al., 1996):

$$S_{inv} = \int_{Z0}^{Z1} S \times dx = \int_{Z0}^{Z1} S_{FeS+FeS_2} \cdot \left(\frac{(1-\varphi) \times \rho}{100 \times M} \right) \times dx, \quad (5)$$

where $S_{FeS+FeS2}$ is a sum of AVS and pyrite sulfur (%dw), φ is porosity of 0.8 (Jørgensen et al., 2001), ρ is average grain density (2.55 g cm^{-3}), M is 32.06 g S mol^{-1}. The sulfide inventory for the FeS_{am}-rich layer of 32 cm width, S_{inv}, is 1.83 mmol S cm^{-2} (mostly AVS), and S_{inv} for the upper 100 cm of Unit III is 14.8 mmol cm^{-2} (mostly FeS_2). The amount of FeS_2 for a layer of 32 cm width in the upper 100 cm of Unit III would be equivalent to 4.89 mmol cm^{-2}. We assume that 1 mol of FeS_2 forms by consumption of 1 mol of AVS sulfur (FeS) and 1 mol of elemental sulfur (S^0 or S_n^{2-}, reaction 1) or 1 mol of H_2S (reaction 3). Thus, if the AVS existing in the FeS_{am}-rich layer converts entirely to pyrite, 1.83×2 = 3.66 mmol cm^{-2} of pyrite S must be formed. This is only 75% of the observed pyrite inventory (3.66/4.89 = 0.75). These calculations suggest that the remaining pyrite (25%) in the upper Unit III sediments is formed without the accumulation of a FeS precursor. The kinetics and mechanisms of pyrite formation under high H_2S concentration in the upper Unit III sediments must be different from the kinetics and mechanisms in the FeS_{am}-rich layer where dissolved sulfide and sulfur intermediates are limiting. In the upper part of Unit III sediment direct pyrite precipitation may occur without a precursor accumulation as proposed by Howarth (1979) and Raiswell (1982). Preexisting pyrite nuclei and/or iron limitation may be essential for this reaction (Harmandas et al., 1998).

To investigate the mechanism of pyrite formation with an iron monosulfide precursor, the chemical composition of the precursor must be known. AVS by definition may include
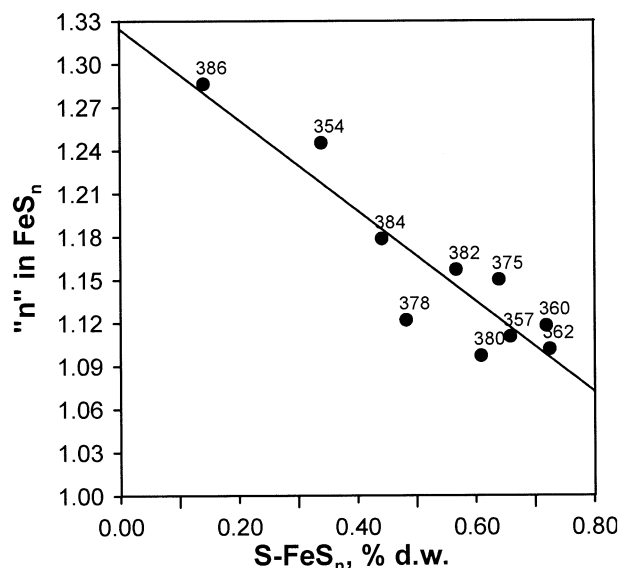

Fig. 9. The relationship between AVS concentration and chemical composition of FeS_n sulfides in the FeS_{am}-rich layer. Indices are sediment depths (cmbsf).

"amorphous" FeS (FeS_{am}), mackinawite $FeS_{0.91–1.10}$ and greigite $FeS_{1.33}$ (Fe_3S_4) (Chanton and Martens, 1985; Morse and Cornwell, 1987). The chemical composition of these compounds can be calculated from the amount of elemental sulfur that forms during the AVS extraction (S^0_{AVS}) (Howarth and Jørgensen, 1984) according to the following stoichiometry (Volkov, 1984):

$$FeS_n + 2H^+ \rightarrow H_2S + (n-1)S^0 + Fe^{2+} \quad (6)$$
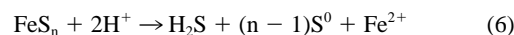
In AVS-rich sediments elemental sulfur can also be formed by the reaction between Fe(III) and H_2S produced during sample acidification (Cornwell and Morse, 1987). However, the extent of Fe(III) interference on H_2S recovery is dependent on the amount of extracted sediment and H_2S stripping rate. Therefore, it becomes significant only at relatively high Fe(III) concentrations (e.g., exceeding 16 mg of goethite per reaction). Our sediment extractions contained several times less total Fe(III) (I. Volkov, unpublished data), and our hot extractions were performed with high gas stripping rate. Therefore, we believe that Fe(III) interference with the H_2S recovery in our samples is insignificant. Our data show that the chemical composition of AVS in the FeS_{am}-rich layer corresponds to the formula $FeS_{1.10–1.29}$ (Fig. 9), which is between the chemical composition of mackinawite and greigite. Our data corroborate the results by Volkov (1984), who showed that iron sulfides in Black Sea micro-nodules containing mackinawite and greigite have also the mean chemical composition corresponding to the formula $FeS_{1.15–1.33}$. The $\delta^{34}S$-AVS and $\delta^{34}S$-S^0_{AVS} of the one nodule extracted from the 343 cmbsf depth were −0.9‰ and −2.2‰, respectively, which are between the isotope composition of the coexisting sulfide of −4.3‰ at 309 cmbsf, the deepest available data point (Jørgensen et al., in press) and the $\delta^{34}S$-AVS value of +8.0‰ at this depth. In addition, the XRD spectrum of the nodule indicated the presence of both greigite and pyrite (Fig. 6).

Earlier studies of Black Sea nodules recovered from the limnic sediment also revealed their mixed composition, with a predominance of mackinawite and greigite and insignificant pyrite contents (Berner, 1974; Volkov, 1984; Bonev et al., 1989). The mechanism of greigite formation and its coexistence with pyrite in the upper limnic sediments in the Black Sea are most probably the same as was described by Jiang et al. (2001) in mudstones from the southwestern Taiwan. These authors observed three different forms of greigite—nodular, framboidal and matrix—where the first two forms were genetically related to partial oxidation and dissolution of pyrite. The third form, matrix greigite, occurred between phyllosilicate layers and was formed subsequent to pyrite.

Mackinawite and greigite in the FeS_{am}-rich layer coexist with an increased elemental sulfur content relative to the above-lying sediments (Fig. 4). The conversion of iron monosulfides to pyrite happens in the uppermost part of FeS_{am}-rich layer and is accompanied by an abrupt drop in AVS and S^0 content, which indicates the essential role of elemental sulfur (or polysulfides in the presence of HS^-) in this process. Wang and Morse (1996) provided experimental evidence that the formation of pyrite is most rapid in the presence of greigite, but a direct conversion of mackinawite to pyrite is also possible (e.g., Schoonen and Barnes, 1991a).

Greigite is a ferromagnetic mineral and its NRM analysis is used in paleomagnetic studies (e.g., Hu et al., 2001; Jiang et al., 2001). Its presence is commonly related to early diagenetic processes. Yet, there are also reports of later diagenetic greigite formation in marine sediments (Roberts and Turner, 1993; Reynolds et al., 1994; Sagnotti and Winkler, 1999) as was demonstrated in the present study. The occurrence of later diagenetic greigite revealed by magnetic and geochemical measurements in the zone of anaerobic methane oxidation can indicate existing and past sulfidization fronts. In deep Amazon Fan sediments, Kasten et al. (1998) also found a close association of greigite with iron-rich layers formed during a secondary overprint caused by anaerobic oxidation of methane. Further studies in other marine sedimentary systems, particularly addressing sedimentary diagenesis during the Pleistocene/Holocene time, might reveal how general the presence of greigite and past and present sulfidization fronts are associated with anaerobic oxidation of methane in marine sediments.

4.2. Iron Relationships

Detailed analyses of the distribution of iron species indicate that sulfidization did not result in significant iron enrichment in association with Fe^{2+} diffusing up into the upper limnic sediment (Table 1). In the FeS_{am}-rich layer, Fe_{total}/Al *(3)* and $Fe_{dith+pyr}/Al$ *(4)* ratios are close to the ratios in sediments above and below. Our data, however, are in contrast with results of Volkov and Tikhomirova (1966), who observed a 3.5-fold increase of total iron in the FeS_{am}-rich layer. The advancement of the sulfidization front is driven by the sulfide flux from above and the amount of total reactive iron present, including the dissolved iron flux from below and, therefore, we believe that, depending on environmental conditions, either situation may occur.

Sulfidization of iron-containing minerals is essentially controlled by the amount of reactive iron as shown above. In situ reductive dissolution and sulfidization of iron minerals dominates the FeS_{am}-rich layer, because the ratios $Fe_{dith+pyr}/Fe_{total}$ *(5)* are not different from those above. However, not all available reactive iron is sulfidized in the AVS-rich layer ($Fe_{AVS+pyr}/Fe_{total}$ *(1)*). Above the FeS_{am}-rich layer a 33% (($31.3–21.1)/31.3 = 0.33$ *(1)*) increase in sulfidized iron is observed. This increase is essentially represented by pyrite iron and is consistent with the DOS values, because the AVS content above the layer is insignificant. This pyrite fraction is formed by direct precipitation without a FeS precursor. These data are well correlated with solid-phase sulfur data (25% of pyrite in the upper limnic sediment are formed by direct precipitation without FeS precursor) (see 4.1).

Summarizing, the general scheme of non–steady-state pyritization in Unit III Black Sea sediments can be described as:

$$Fe(II, III) + HS^- \rightarrow FeS_n(Fe_3S_4) \rightarrow FeS_2 \qquad (7)$$
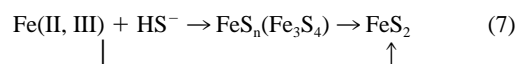
The first stages of the process are the reactions in the sediment pore water between hydrogen sulfide and reduced iron in solution and in the solid phase (mostly ferrous iron of silicates and carbonates). The second step is reaction between sulfide and Fe(III)-containing oxides and clay minerals generating S^0 and AVS (Pyzik and Sommer, 1981; Afonso and Stumm, 1992; Peiffer et al., 1992). Metastable iron sulfides in the hydrotrolite layer have a chemical composition of $FeS_{1.10–1.29}$, and probably represent a mixture of stoichiometric mackinawite and greigite.

Sulfidization of acid-volatile sulfides to pyrite is the terminal step of the AVS conversion to pyrite. According to Volkov (1984), the conversion of AVS to pyrite is controlled by the S^0/AVS mass ratio and would be favored at Station 7 when the ratio is more than 0.5–0.6 (data not shown). Pyrite precipitation from the FeS_n precursors is mediated by sulfur intermediates (e.g., Rickard, 1975; Luther, 1991) or, as suggested by Rickard (1997), directly by H_2S. AVS conversion into pyrite is controlled by the AVS solubility product, which in turn depends on Fe^{2+} and S^{2-} concentrations and pH. Overall, the AVS enrichment in deep Black Sea sediments is a transient phenomenon, since pyrite is the main form of TRS in the upper part of Unit III sediments overlying the FeS_{am}-rich layer. This situation is different from secondary diagenetic processes described by Gagnon et al. (1995) in Saguenay Fjord sediments. In contrast to the Black Sea, pyrite formation in those anoxic sediments was sulfide-limited, and Fe^{2+} in the sediment pore water was in excess with concentrations of 720 μM. Under such conditions, the conversion of AVS to pyrite was apparently retarded due to a lack of intermediate reduced sulfur species and ΣH_2S. Once pyrite has formed through nucleation and subsequent sulfidization of an iron monosulfide precursor, it can serve as a nucleus for a direct precipitation from solution (Wang and Morse, 1996; Harmandas et al., 1998; Benning et al., 2000).

4.3. Sulfur Isotope Composition of Reduced Sulfur Species as an Indicator of Diagenetic Transformations

Based on the vertical profile of $\delta^{34}S$-FeS_2 the core can be divided into two parts—one above and one below the interface

between Holocene and late Pleistocene sediments (Unit IIb/III). Although the scatter of δ^{34}S-FeS$_2$ in the upper part of the core is significant (up to 26.4‰), the values are generally below −20‰, which is typical for sedimentary sulfides formed under marine conditions with an excess of sulfate.

A significant enrichment in ^{34}S in the pyrite of the uppermost part of the limnic clays, with δ^{34}S values of up to +15.0‰, is a clear indication of a secondary diagenetic overprint. The limnic sediments below the hydrotrolite layer have an average δ^{34}S-FeS$_2$ of −3.5‰ (Fig. 7a), which is in the range reported by other authors for late Pleistocene Black Sea sediments unchanged by later diagenetic processes (Vinogradov et al., 1962; Nikolaev, 1995; Calvert et al., 1996). A highly ^{34}S-enriched pyrite could only be formed from isotopically heavy dissolved sulfide because the sulfur fractionation during iron sulfide precipitation is only minor (e.g., Böttcher et al., 1998a; Wilkin and Barnes, 1996; Butler et al., 2000). In addition, this isotopically "heavy" sulfide cannot have formed within the sapropel, because the δ^{34}S-FeS$_2$ in the sapropel (Unit IIa) is < −20‰. Pore water profiles of H$_2$S also argue against hydrogen sulfide diffusion from the sapropel into the limnic clays (e.g., Berner, 1974; Volkov, 1984). Therefore, the observed isotope composition of solid phase sulfur species will be influenced by the isotope composition of initial sulfate and the net fractionation factor during AMO (Aharon and Fu, 2000; Böttcher et al., 2000). In addition to these factors, δ^{34}S-FeS$_2$ in the upper limnic sediment is a cumulative product of pyrite formed over time during (i) growth from FeS$_n$ precursors and (ii) by direct precipitation during different stages of the secondary diagenetic overprint. The model explaining the isotopically heavy pyrite formation in the upper Pleistocene sediments is presented in a companion paper by Jørgensen et al. (in press).

4.4. Hydrogen Sulfide Source and the Advancement of a Sulfidization Front

H$_2$S budget calculations by Jørgensen et al. (in press) show that the net sulfate reduction in the AMO zone at Station 7 is 40.2 mmol m^{-2} yr^{-1}. Of the H$_2$S formed, 8.4 mmol m^{-2} yr^{-1} (21%) diffuses up, 8.8 mmol m^{-2} yr^{-1} (22%) diffuses down, and the rest, 23.0 mmol m^{-2} yr^{-1} (57%), is trapped by reaction with iron and by immobilization as elemental sulfur and organic sulfur. Overall, sulfide production due to deep sulfate reduction in the AMO zone at this station accounts for 79% (22% + 57% = 79%) of the combined sulfide flux and sulfur immobilization in the upper limnic clays. Methane, however, constitutes only 44% of the substrate for sulfate reduction at these depths. At shallower stations methane consumption corresponded to 62–102% of the sulfate reduction in the sulfate-methane transition zone (Jørgensen et al., 2001).

Advancement of the sulfidization front in the upper Unit III sediments can be described by the steady-state model developed by Berner (1969) for sediments with contrasting C$_{org}$-Fe$_{react}$ chemistries. This approach was successfully applied to investigate sulfidization processes in Ancylus clays in the Baltic Sea (Boesen and Postma, 1988). Depending on the amount of reactive iron available, Berner (1969) considered three modes of iron sulfide formation at the interface between high organic matter sediments and low organic matter sediments—namely, low iron, high iron and Liesegang (intermediate) sit-

uations. Sulfidization of the upper Black Sea limnic sediments best fits the "low iron" scenario, because continuous downward flux of sulfide persists over time.

Under stationary conditions for the H$_2$S and Fe^{2+} fluxes, the time, T, for the iron sulfide front advancement can be calculated as:

$$T = \frac{L^2 \times (\sqrt{\pi}[Fe_{sulfide}] \times K + \varphi \times [HS^-]_0)}{4 \times \varphi \times [HS^-]_0 \times D_{HS^-} \times M}, \quad (8)$$

where L is the present location of the sulfidization front (in our case L is the distance between the upper Unit III boundary at 254 cmbsf and the lower part of the FeS$_{am}$-rich layer at 383 cmbsf). The low TRS concentration below 383 cmbsf is similar to the composition of typical limnic clays and was assumed in the model to delineate the lower boundary of the iron sulfidization front (Fig. 4, dashed line). Fe$_{sulfide}$ in Eqn. 8 is the Fe$_{AVS+pyr}$ concentration in mol cm^{-3}. K is the number of moles of sulfide that react with one mole of iron to form iron sulfide: K = 1 for Fe(II)→AVS, or K = 2 for Fe(II)→FeS$_2$. For K = 1, Fe$_{sulfide}$ is 125 μmol cm^{-3} for the AVS layer only, and Fe$_{sulfide}$ is 178 μmol cm^{-3} from the upper Unit III boundary down to the top of the FeS$_{am}$-rich layer. φ is porosity, which ranges in the upper limnic clays between 0.66 and 0.77 (Jørgensen et al., 2001). With a correction for sediment compaction, the value 0.8 is used in the model. The whole sediment diffusion coefficient, D$_{HS^-}$, for dissolved sulfide is 0.9 10^{-5} cm^2 s^{-1}. The coefficient was calculated based on porosity (0.8), temperature (9°C), and salinity (17.5‰) (Jørgensen et al., 2001) according to Boudreau (1997). The HS$^-$ concentration, [HS$^-$]$_O$, is 0.641 ± 0.063 μmol cm^{-3} pore water, which corresponds to the average HS$^-$ concentration above ca. 250 cmbsf (Fig. 2b).

The first calculation was run assuming K = 2 for the upper 97 cm where pyrite is the main form of TRS, and with K = 1 for the lower 32 cm, where AVS is the main form of TRS. In this approach the average content of Fe$_{sulfide}$ in the upper part of Unit III above the FeS$_{am}$-rich layer was assumed to be the same as the AVS content of the FeS$_{am}$-rich layer. In a second model run, we assumed that the sulfidization front advanced only through AVS formation (K = 1 for the whole layer from 254–383 cmbsf).

The estimated times for front advancement are 10610 yr and 6360 yr for the first (K = 1) and second (K = 2) models, respectively. We infer that the advancement should be controlled mostly by the initial Fe sulfidization, i.e., AVS precipitation. Pyrite formation above the FeS$_{am}$-rich layer must proceed over a longer time scale than the AVS precipitation. Thus, the second model should approximate natural conditions more closely than the first one.

The second way to estimate the time, T, for sulfide front advancement is based on a mass balance calculation under steady-state conditions of HS$^-$ flux and the reduced sulfur inventory:

$$T = \frac{S_{inv}}{J_{HS^-}} \quad (9)$$

$$S_{inv} = TRS_{av} \times \frac{(1 - \varphi) \cdot \rho}{100 \times M} \quad (10)$$

$$J_{HS^-} = \varphi \times D_{HS^-} \frac{\partial HS^-}{\partial z} \qquad (11)$$

S_{inv} is the TRS inventory in the upper part of Unit III sediments. J_{HS^-} is the HS^- vertical flux in the sulfate/methane transition zone. TRS_{av} is the average concentration of TRS, including the HS^- content in pore waters in %dw. All other terms in the equation are the same as in Eqn. 8. The S_{inv} (Eqn. 10) for Station 7 is 15.84 mmol cm^{-2}. The initial content of TRS in the limnic sediment was not considered, because the TRS content in the limnic clays below the FeS_{am}-rich layer did not exceed 0.1% d.w. The H_2S immobilization rate calculated by Jørgensen et al. (in press) for Station 7 is 23.0 mmol m^{-2} yr^{-1}. Thus, under steady-state conditions for the H_2S flux over time, the time (T) for the front advancement is ~6900 yr, which is fairly close to the second estimate resulting from the Berner (1969) model.

For both calculations we assumed the sulfate-sulfide-methane gradients to be steady-state over time. Our results indicate that the process of secondary sulfidization of limnic clays in the Black Sea started more likely either with the beginning of the marine phase approximately 7150–9800 yr BP (Jones and Gagnon, 1994; Lane-Serff et al., 1997; Ryan et al., 1997; Arthur and Dean, 1998) or some time after the beginning of the sapropel deposition, 7540 yr BP, when sulfide had already started to build up in the water column (Jones and Gagnon, 1994).

We are aware that the steady-state assumptions made for these calculations may not be realistic if the sulfate/methane system is far from steady-state. Possible changes in sulfate and methane fluxes during late Pleistocene/Holocene are the main factors for the diffusion-diagenesis Fe-S system in the upper limnic sediment being at not steady-state. In addition, non–steady-state situations can be caused by turbidites or erosion, which are common events along the continental margins and also on the Black Sea continental slope.

Models for evolving Black Sea salinity after the opening of Bosporus shows that salinity (and also sulfate) in bottom waters reached 90% of present-day values ~2500 yr after the opening (Karaca et al., 1999) or indicate that the freshwater content of the Black Sea became totally depleted over a period of ~3700 yr after the opening (Lane-Serff et al., 1997). The presence of bacteriochlorophylls in Black Sea sediments younger than 6200 yr BP (Sinninghe Damsté et al., 1993) indirectly indicates that at the beginning of the sapropel deposition the location of the Black Sea chemocline (and the whole hydrophysical structure of the water column) generally reached the present-day conditions. Therefore, changes in sulfate concentration in the water column during the early Holocene may have influenced the intensity of AMO only during the first 2500 yr or shorter. Jørgensen et al. (in press) calculated that the characteristic diffusion time required to form the present-day sulfate profile at Station 7 is ~560 yr, which is short compared with the salinity development in the Black Sea (2500 yr). The carbon isotope composition of methane diffusing up into overlying sediment indicates its microbial origin (Böttcher, unpublished data). Therefore, the opening of the Bosporus most likely had a minor influence on the upward flux of methane. Although gas hydrates have been found in subbottom Black Sea sediments (40–220 cmbsf) at a water depth of 2000 m, they are located mostly in the central parts of the basin (Ginzburg et al., 1990) and are of no importance in the study area. Hence, the location of the sulfate-methane transition has probably been relatively constant over the Holocene.

The sulfate and methane flux calculations indicate that sulfide production in the upper Pleistocene sediments at Station 7 is mostly driven by AMO (Jørgensen et al., in press). The location of the sulfate-methane transition has been stable over the Holocene. Our model calculations show that the advancement of the sulfidization front initiated around the time of the Pleistocene/Holocene transition. If all three assumptions are valid, the present location of the sulfate-methane interface near the Unit II/III boundary must be dictated by the relative fluxes of CH_4 and SO_4^{2-}. It is indeed located near this boundary (Fig. 2a). Thus, we believe that our model calculations provide realistic estimates for the timing of the ongoing sulfidization process.

5. CONCLUSIONS

Progressive pyritization in late Pleistocene sediments of the Black Sea is induced by diffusion of sulfide formed by anaerobic methane oxidation and ultimately linked to sulfate diffusion. According to steady-state model calculations, advancement of the sulfidization front started between 6360 and 11600 yr BP and was therefore coincident with the beginning of marine phase 7150–9800 yr ago. The advancement of a sulfidization front in the Upper Pleistocene sediments is an ongoing process.

The advancement of the sulfidization front in the upper limnic sediment is not associated with iron accumulation but rather with partitioning between iron mineral solid phases. Two different pyritization processes in the upper part of the Black Sea Pleistocene clays were identified. The first process includes pyrite precipitation with the accumulation of FeS_n precursors. They are characterized by a chemical composition between $FeS_{1.10}$ and $FeS_{1.29}$, indicating a mixture of mackinawite and greigite. Elemental sulfur formed by reductive dissolution of iron (III)-containing oxides present in the limnic sediment serves as an intermediate to convert AVS to pyrite. In the second mechanism, pyrite originates from exposure of iron (II)-containing minerals to dissolved sulfide and most likely precipitates on a pyrite precursor ("seed") without the formation of a FeS_n precursor. Greigite formed either as the intermediate during AVS conversion to pyrite or subsequently from pyrite by its partial dissolution and oxidation. Our study stresses the importance of greigite formation as an indicator of the present and past sulfidization front(s) driven by anaerobic methane oxidation.

Progressive formation of pyrite is reflected in changes in its isotopic composition due to contributions of different sulfur pools formed at different times. The isotopic composition of sulfur species in a system driven by anaerobic methane oxidation is determined by several factors. Among them are depth shifts in the sulfate/methane transition mostly controlled by the methane flux, changes in sedimentation rates or in the sulfur isotope fractionation factor during methane oxidation, and the occurrence of turbidites or erosion events.

The pyrite concentrations and isotope signatures in ancient rocks are commonly considered to represent the initial condi-

tions of deposition during early diagenetic processes. In this paper and in a companion paper by Jørgensen et al. (in press) we report results demonstrating that the $\delta^{34}S$ of Black Sea deep sediments and the entire S-Fe chemistry are significantly altered by a secondary diagenetic overprint occurring well below the present zone of sulfate reduction through HS^- diffusion. There is growing evidence from continental margin sediments and continental strata that non–steady state diagenetic processes have a high potential for producing and preserving S-enriched layers (Kirkland et al., 1995; Kasten et al., 1998; Böttcher et al., unpublished data). In all reported cases, such diagenetic enrichments were induced by sulfide production during anaerobic methane oxidation. Anaerobic methane oxidation is a quantitatively important bacterial activity in subseafloor sediments as recently reviewed by Parkes et al. (2000). Thus, the situation described for sediments of the Black Sea may have broader paleoenvironmental importance.

Associate editor: D. Canfield

REFERENCES

Afonso M. D. and Stumm W. (1992) Reductive dissolution of iron (III) (hydr)oxides by hydrogen sulfide. *Langmuir* **8,** 1671–1675.

Aharon P. and Fu B. (2000) Microbial sulfate reduction rates and sulfur and oxygen isotope fractionations at oil and gas seeps in deepwater Gulf of Mexico. *Geochim. Cosmochim. Acta* **64,** 233–246.

Arthur M. A. and Dean W. (1998) Organic-matter production and preservation and evolution of anoxia in the Holocene Black Sea. *Paleoceanography* **13,** 395–411.

Benning L. G., Wilkin R. T., and Barnes H. L. (2000) Reaction pathways in the Fe-S system below 100 degrees C. *Chem. Geol.* **167,** 25–51.

Berner R. (1969) Migration of iron and sulfur within anaerobic sediments during early diagenesis. *Am. J. Sci.* **267,** 19–42.

Berner R. (1970) Sedimentary pyrite formation. *Am. J. Sci.* **268,** 1–23.

Berner R. (1974) Iron sulfides in Pleistocene deep Black Sea sediments and their paleo-oceanographic significance. In *The Black Sea: Geology, Chemistry and Biology* (eds. E. T. Degens and D. A. Ross), pp. 524–531. American Association of Petroleum Geologists.

Boesen C. and Postma D. (1988) Pyrite formation in anoxic environments of the Baltic. *Am. J. Sci.* **288,** 575–603.

Bonev I. K., Khrischev Kh. G., Neikov H. N., and Georgiev V. M. (1989) Mackinawite and greigite in iron sulphide concretions from Black Sea sediments. *Doklady Bolgarskoy Akademii Nauk.* **42,** 97–100.

Böttcher M. E., Smock A. M., and Cypionka H. (1998a) Sulfur isotope fractionation during experimental precipitation of iron (II) and manganese (II) sulfide at room temperature. *Chem. Geol.* **146,** 127–134.

Böttcher M. E., Oelschläger B., Höpner T., Brumsack H.-J., and Rullkötter J. (1998b) Sulfate reduction related to the early diagenetic degradation of organic matter and "black spot" formation in tidal sandflats of the German Wadden Sea (southern North Sea): Stable isotope (^{13}C, ^{34}S, ^{18}O) and other geochemical results. *Org. Geochem.* **29,** 1517–1530.

Böttcher M. E., Boetius A., and Rickert D. (2000) Sulfur isotope biogeochemistry of intense sulfate reduction associated with anaerobic methane oxidation. *J. Conf. Abstr.* **5,** 254–255.

Böttcher M. E. and Lepland A. (2000) Biogeochemistry of sulfur in a sediment core from the west-central Baltic Sea: Evidence from stable isotopes and pyrite textures. *J. Mar. Systems* **25,** 299–312.

Boudreau B. (1997) *Diagenetic Models and Their Implementation: Modelling Transport and Reactions in Aquatic Sediments.* Springer-Verlag.

Butler I., Böttcher M. E., and Rickard D. (2000) Sulfur isotope discrimination during experimental formation of pyrite. *J. Conf. Abstr.* **5,** 272–273.

Calvert S. E., Thode H. G., Yeung D., and Karlin R. E. (1996) A stable isotope study of pyrite formation in the late Pleistocene and Holocene sediments of the Black Sea. *Geochim. Cosmochim. Acta* **60,** 1261–1270.

Canfield D. E. (1989) Reactive iron in marine sediments. *Geochim. Cosmochim. Acta* **53,** 619–632.

Canfield D. E., Raiswell R., and Bottrell S. (1992) The reactivity of sedimentary iron minerals toward sulfide. *Am. J. Sci.* **292,** 659–683.

Canfield D. E., Lyons T., and Raiswell R. (1996) A model for iron deposition to euxinic Black Sea sediments. *Am. J. Sci.* **296,** 818–834.

Chanton J. P. and Martens C. S. (1985) The effects of heat and stannous chloride addition on the active distillation of acid volatile sulfide from pyrite-rich marine sediment samples. *Biogeochemistry* **1,** 375–383.

Cline J. D. (1969) Spectrophotometric determination of hydrogen sulfide in natural waters. *Limnol. Oceanogr.* **14,** 454–458.

Cornwell J. C. and Morse J. W. (1987) The characterization of iron sulfide minerals in anoxic marine sediments. *Mar. Chem.* **22,** 193–206.

Drobner E., Huber H. J., Wächterhauser G., Rose D., and Stetter K. O. (1990) Pyrite formation linked with hydrogen evolution under anaerobic conditions. *Nature* **246,** 742–744.

Gagnon C., Mucci A., and Pelletier E. (1995) Anomalous accumulation of acid-volatile sulphides (AVS) in a coastal marine sediment, Saguenay Fjord, Canada. *Geochim. Cosmochim. Acta* **59,** 2663–2675.

Ginzburg G., Kremlev A. N., Grigoriev M. N., Larkin G. V., Pavlenkin A. D., and Saltykova N. A. (1990) Filtrogenic gas hydrates in the Black Sea (21 voyage of the research vessel Evpatoriya). *Geol. Geophyz.* **313,** 10–19.

Harmandas N. G., Navarro Fernandez E., and Koutsoukos P. G. (1998) Crystal growth of pyrite in aqueous solutions, inhibition by organophosphorus compounds. *Langmuir* **14,** 1250–1255.

Hay B. J., Arthur M. A., Dean W. E., Neff E. D., and Honjo S. (1991) Sediment deposition in the Late Holocene abyssal Black Sea with climatic and chronological implications. *Deep-Sea Res.* **II38,** S1237–S1254.

Howarth R. W. (1979) Pyrite: Its rapid formation in a salt marsh and its importance in ecosystem metabolism. *Science* **203,** 49–51.

Howarth R. W. and Jørgensen B. B. (1984) Formation of ^{35}S-labelled elemental sulfur and pyrite in coastal marine sediments (Limfjorden and Kysing Fjord, Denmark) during short-term $^{35}SO_4^{2-}$ reduction measurements. *Geochim. Cosmochim. Acta* **48,** 1807–1818.

Hu Y., Oldfield F., Manalt F., and Beck C. (2001) The environmental significance of magnetic measurements of late Pleistocene and Holocene sediments from the Grand Lac d'Annecy, Eastern France. *J. Paleolimnol.* **25,** 193–203.

Hurtgen M. T., Lyons T. W., Ingall E. D., and Cruse A. M. (1999) Anomalous enrichments of iron monosulfide in euxinic marine sediments and the role of H_2S in iron sulfide transformations: Examples from Effingham Inlet, Orca Basin, and the Black Sea. *Am. J. Sci.* **299,** 556–588.

Jiang W.-T., Horng C.-S., Roberts A. P., and Peacor D. R. (2001) Contradictory magnetic polarities in sediments and variable timing

of neoformation of authigenic greigite. *Earth Planet. Sci. Lett.* **193**, 1–12.

Jones G. A. and Gagnon A. (1994) Radiocarbon chronology of Black Sea sediments. *Deep-Sea Res.* **I41**, 531–557.

Jørgensen B. B. (1977) The sulfur cycle of a coastal marine sediment. *Limnol. Oceanogr.* **22**, 814–832.

Jørgensen B. B., Weber A., and Zopfi J. (2001) Sulfate reduction and anaerobic methane oxidation in Black Sea sediments. *Deep-Sea Res.* **48**, 2097–2120.

Jørgensen B. B., Böttcher M. E., Lüschen H., Neretin L., and Volkov I. I. (2004) Anaerobic methane oxidation and a deep H_2S sink generate isotopically heavy sulfides in Black Sea sediments. *Geochimica Cosmochimica Acta* 68(9), 2095–2118.

Karaca M., Wirth A., and Ghil M. (1999) A box model for the paleoceanography of the Black Sea. *Geophys. Res. Lett.* **26**, 497–500.

Kasten S., Freudenthal T., Gingele F. X., and Schulz H. D. (1998) Simultaneous formation of iron-rich layers at different redox boundaries in sediments of the Amazon deep-sea fan. *Geochim. Cosmochim. Acta* **62**, 2253–2264.

Kirkland D. W., Denison R. E., and Rooney M. A. (1995) Diagenetic alteration of permian strata at oil fields of South Central Oklahoma, USA. *Mar. Petrol. Geol.* **12**, 629–644.

Kozerenko S. V., Khramov D. A., Fadeev V. V., Kalinichenko A. M., Marov I. N., Evtikova D. A., and Rusakov V. S. (1995) Studies of pyrite formation mechanisms in aqueous solutions at low temperatures and pressures (in Russian, English translation). *Geokhimiya* **9**, 1352–1366.

Lane-Serff G. F., Rohling E. G., Bryden H. L., and Charnock H. (1997) Postglacial connection of the Black Sea to the Mediterranean and its relation to the timing of sapropel formation. *Paleoceanography* **12**, 169–174.

Lüschen H. (1998) High-resolution geochemical analysis of a sediment core from the Black Sea. Diplom. thesis. University of Oldenburg.

Luther G. I. III. (1991) Pyrite synthesis via polysulphide compounds. *Geochim. Cosmochim. Acta* **55**, 2839–2849.

Lyons T. W. (1997) Sulfur isotopic trends and pathways of iron sulfide formation in upper Holocene sediments of the anoxic Black Sea. *Geochim. Cosmochim. Acta* **61**, 3367–3382.

Lyons T. W., Werne J. P., Hollander D. J., and Murray R. W. (2003) Contrasting sulfur geochemistry and Fe/Al and Mo/Al ratios across the last oxic-to-anoxic transition in the Cariaco Basin, Venezuela. *Chem. Geol.* **195**, 131–157.

Middelburg J. J. (1991) Organic carbon, sulfur and iron in recent semi-euxinic sediments of Kau Bay, Indonesia. *Geochim. Cosmochim. Acta* **55**, 815–828.

Morse J. W. and Cornwell J. C. (1987) Analysis and distribution of iron sulfide minerals in recent anoxic marine sediments. *Mar. Chem.* **22**, 55–69.

Neretin L. N., Volkov I. I., Böttcher M. E., and Grinenko V. A. (2001) A sulfur budget for the Black Sea anoxic zone. *Deep- Sea Res. I* **48**, 2569–2593.

Nikolaev S. (1995) *Isotopic Paleoceanography of Inter-Continental Basins* (in Russian). VNIRO, Moscow.

Parkes R. J., Cragg B. A., and Wellsbury P. (2000) Recent studies on bacterial populations and processes in subseafloor sediments: A review. *Hydrogeol. J.* **8**, 11–28.

Passier H. F., Middelburg J., van Os B. J. H., and de Lange G. J. (1996) Diagenetic pyritisation under eastern Mediterranean sapropels caused by downward sulphide diffusion. *Geochim. Cosmochim. Acta* **60**, 751–763.

Passier H. F., Middelburg J. J., de Lange G. J., and Böttcher M. E. (1999) Modes of sapropel formation in the eastern Mediterranean: Some constraints based on pyrite properties. *Mar. Geol.* **153**, 199–219.

Peiffer S., Afonso M. S., Wehrli B., and Gächter R. (1992) Kinetics and mechanism of the reaction of H_2S with lepidocrite. *Environ. Sci. Technol.* **26**, 2408–2413.

Postfai M., Buseck P. R., Bazylinski D. A., and Frankel R. B. (1998) Reaction sequence of iron sulfide minerals in bacteria and their use as biomarkers. *Science* **280**, 880–883.

Pyzik A. J. and Sommer S. E. (1981) Sedimentary iron monosulfides: Kinetics and mechanism of formation. *Geochim. Cosmochim. Acta* **45**, 687–698.

Raiswell R. (1982) Pyrite texture, isotopic composition and availability of iron. *Am. J. Sci.* **282**, 1244–1263.

Raiswell R., Canfield D. E., and Berner R. A. (1994) A comparison of iron extraction methods for the determination of degree of pyritization and the recognition of iron-limited pyrite formation. *Chem. Geol.* **111**, 101–110.

Reynolds R. L., Tuttle M. L., Rice C. A., Fishman N. S., Karachewski J. A., and Sherman D. M. (1994) Magnetization and geochemistry of greigite-bearing Cretaceous strata, North Slope Basin, Alaska. *Am. J. Sci.* **294**, 485–528.

Rickard D. (1975) Kinetics and mechanism of pyrite formation at low temperatures. *Am. J. Sci.* **275**, 636–652.

Rickard D. (1995) Kinetics of FeS precipitation; part 1, competing reaction mechanisms. *Geochim. Cosmochim. Acta* **59**, 4367–4379.

Rickard D. (1997) Kinetics of pyrite formation by the H_2S oxidation of Fe(II) monosulfide in aqueous solutions between 25 and 125°C: The rate equation. *Geochim. Cosmochim. Acta* **61**, 115–134.

Rickard D. and Luther G. III. (1997) Kinetics of pyrite formation by the H_2S oxidation of Fe(II) monosulfide in aqueous solutions between 25 and 125°C: The mechanism. *Geochim. Cosmochim. Acta* **61**, 135–147.

Roberts A. P. and Turner G. M. (1993) Diagenetic formation of ferrimagnetic iron sulfide minerals in rapidly deposited marine sediments, South Island, New Zealand. *Earth Planet. Sci. Lett.* **115**, 257–273.

Rozenson I. and Heller-Kallai L. (1976) Reduction and oxidation of Fe^{3+} in dioctahedral smectites—2: Reduction with sodium sulphide solutions. *Clays Clay Miner.* **24**, 283–288.

Ryan W. G. F., Pitman I. W., Major C. O., Shimkus K., Moskalenko V., Jones J. A., Dimitrov P., Gorur N., Sakinc M., and Yuce H. (1997) An abrupt drowning of Black Sea shelf. *Mar. Geol.* **138**, 119–126.

Sagnotti L. and Winkler A. (1999) Rock magnetism and palaeomagnetism of greigite-bearing mudstones in the Italian peninsula. *Earth Planet. Sci. Lett.* **165**, 67–80.

Schoonen M. A. A. and Barnes H. L. (1991a) Reactions forming pyrite and marcasite from solution: I. Nucleation of FeS_2 below 100°C. *Geochim. Cosmochim. Acta* **55**, 1495–1504.

Schoonen M. A. A. and Barnes H. L. (1991b) Reactions forming pyrite and marcasite from solution: II. Via FeS precursors below 100°C. *Geochim. Cosmochim. Acta* **55**, 1505–1514.

Sinninghe Damsté J., Wakeham S. G., Kohnen M. E. L., Hayes J. M., and de Leeuw J. W. (1993) A 6,000-year sedimentary molecular record of chemocline excursions in the Black Sea. *Nature* **362**, 827–829.

Strakhov N. I. (1963) About some new data on the Black Sea sediments diagenesis. *Lithol. Mineral Dep.* **1**, 7–27.

Sweeney R. E. and Kaplan I. R. (1973) Pyrite framboid formation: Laboratory synthesis and marine sediments. *Econ. Geol.* **68**, 618–634.

Verosub K. L. and Roberts A. P. (1995) Environmental magnetism: Part, present, and future. *J. Geophys. Res.* **100**, 2175–2192.

Vinogradov A. P., Grinenko V. A., and Ustinov V. I. (1962) Isotopic composition of sulphur compounds in the Black Sea. *Geokhimiya* **10**, 973–997.

Volkov I. I. (1964) Iron sulfide nodules in the Black Sea sediments: Formation and chemical composition (in Russian). *Trudy Inst. Okeanol.* **67**, 101–134.

Volkov I. I. (1984) *Sulphur Geochemistry of Ocean Sediments* (in Russian). Nauka.

Volkov I. I. and Tikhomirova A. A. (1966) Iron forms in the oxic Black Sea sediments. *Lithol. Min. Dep.* **4**, 24–37.

Volkov I. I., Zhabina N. N., Sokolov V. S., Demidova T. P., Morozov A. A., and Pushkina Z. V. (1981) Sulfur compounds in sediments of the Arabian part of the Indian Ocean. *Geokhimiya* **10**, 1569–1590.

Wang Q. and Morse J. W. (1996) Pyrite formation under conditions approximating those in anoxic sediments. I. Pathway and morphology. *Mar. Chem.* **52**, 99–121.

Wilkin R. T. and Barnes H. L. (1996) Pyrite formation by reactions of iron monosulfides with dissolved inorganic and organic sulfur species. *Geochim. Cosmochim. Acta* **60,** 4167–4179.

Wilkin R. T., Arthur M. A., and Dean W. E. (1997) History of water-column anoxia in the Black Sea indicated by pyrite framboid size distributions. *Earth Planet. Sci. Lett.* **148,** 517–525.

Wilkin R. T. and Arthur M. A. (2001) Variations in pyrite texture, sulfur isotope composition, and iron systematics in the Black Sea: Evidence for late Pleistocene to Holocene excursions of the O_2-H_2S redox transition. *Geochim. Cosmochim. Acta* **65,** 1399–1416.

Zhabina N. N. and Volkov I. I. (1978) A method of determination of various sulfur compounds in sea sediments and rocks. In *Environmental Biochemistry and Geomicrobiology*, Vol. 3, *Methods, Metals, and Assessment* (ed. W. E. Krumbein), pp. 735–746. Ann Arbor Science.